Int. J. Heat Mass Transfer. Vol. 36, No. 4, pp. 857–873, 1993
Printed in Great Britain

0017–9310/93 $6.00 + 0.00
Pergamon Press Ltd

Two-dimensional modelling of a non-confined circular impinging jet reactor—fluid dynamics and heat transfer

Y. B. WANG, C. CHAUSSAVOINE and F. TEYSSANDIER

CNRS, Institut de Science et de Génie des Matériaux et Procédés, Université-Avenue de Villeneuve, F-66860 Perpignan Cédex, France

(*Received* 12 *December* 1991 *and in final form* 23 *May* 1992)

Abstract—Coupled momentum and heat transfers have been numerically studied in a non-confined, axisymmetrical, laminar, and initially cold jet impinging on a flat substrate heated at high temperature. Variable physical properties were taken into account. The flow field as well as the local heat transfer rate was studied as a function of various parameters such as Reynolds and Froude numbers, nozzle-substrate distance, substrate temperature, and jet directions (upwards, downwards). The calculated flow field as well as the local Nusselt number are in good accordance with the experimental data from the literature at low temperature difference between the gas and the substrate. The numerical solution describes satisfactorily the non-monotonous experimental radial variation of the Nusselt number at small nozzle-substrate distance.

INTRODUCTION

CHEMICAL vapor deposition (CVD) is a versatile method which allows the growth of a wide variety of materials (pure elements, compounds, solid solutions or composite materials) as thin films on various substrates. In this process, a mixture of gases flows around a heated surface where the chemical reactions occur. As a consequence, the thickness or composition homogeneity of the film is highly dependent on gas transport phenomena. A large variety of reactors with various shapes and sizes is currently used in research laboratories and for industrial applications. They can be classified in two main groups: hot-wall and cold-wall reactors. In the latter case, only the substrate is heated and the main feature of these reactors is the large thermal gradient (up to 1000°C cm^{-1}) encountered in the vicinity of the hot substrate. The resulting buoyancy-driven flow recirculations, even under reduced pressure, strongly affect the fluid flow, necessitating an accurate description of the hydrodynamics. Moreover, the heat transfer coupled with the fluid flow may promote homogeneous reactions leading to a modification of the molecules responsible for growth and must be characterized.

In the last seven years it has become clear that the properties of the deposited film (thickness and composition homogeneity, morphology, etc.) strongly depend on gas-phase transportation and therefore on the geometry of the reactor. Experimental systems such as the rotating disk, stagnation point flow and impinging jet present simple and well-defined two-dimensional flow fields which can be made one dimensional in the vicinity of the axis by suitable transformations [1]. The high efficiency of the heat and mass transfers in an impinging jet reactor is a very attractive feature and the fluid flow and heat transfer occurring in a non-confined geometry are numerically studied in this paper.

Many experiments have been carried out on fluid dynamics and heat transfer in a non-confined impinging jet. Tuve [2] studied the velocity distribution from the exit of the nozzle, and Elrod [3] established a diagram which allows the centre velocity of the jet to be calculated as a function of the source velocity. The rate of entrainment of the environmental fluid was studied by Donald and Singer [4]. The heat transfer was also investigated experimentally, by Hrycak [5] between a circular jet and a flat plate or by Gardon and Akrifat [6] between a flat plane and a set of jets. Sparrow *et al.* [7] studied the heat transfer for a circular jet impinging on a confined disk with annular collection of spent air. A synthetical survey dealing with the empirical correlations of Nusselt number in the fluid–solid interface resulting from these experimental results has been given by Martin *et al.* [8] for the uniform turbulent jet.

However, such correlations are only valid in restricted domains of the parameter variation and account for the transport phenomena only at the fluid–solid interface though the knowledge of fluid and temperature fields in the whole fluid phase is required to simulate the gas-phase chemical reactions involved in a CVD process. Furthermore, all these studies are devoted to the turbulent case for large Reynolds numbers, though laminar flow is mostly encountered in CVD.

Classically, analytical solutions are used to solve the mechanical and thermal equations assuming important simplifications such as inviscid fluid [9, 10], or the boundary layer theory [11–13]. More recently, large scale computing models have been developed in

NOMENCLATURE

C_p specific heat at constant pressure [J kg^{-1} K^{-1}]
C_{p0} C_p value at the nozzle entrance [J kg^{-1} K^{-1}]
C_v specific heat at constant volume [J kg^{-1} K^{-1}]
f_1, f_2, f_3 parameters for heating mode on the substrate surface
Fr Froude number, V_{max0}^2/gR_0
G $(1/Fr)(T_v - T_0)/T_0$
g universal acceleration, 9.80655 m s^{-2}
H nozzle–substrate distance [m]
H_u length of the nozzle considered in the calculation, $H_T - H$ [m]
H_T height of the total calculation domain [m]
h distance from the surface of the substrate, $H_T - z$ [m]
J 0, hypothetical case: when the gravity is absent; 1, when the jet is upward facing; -1, when the jet is downward facing
k_H local heat transfer coefficient [J K^{-1} m^{-2} s^{-1}]
M molar mass of gas [g mole^{-1}]
Nu local Nusselt number, $k_H R_0/\lambda_0$
Nu_0 Nusselt number at the centre of the substrate
Nu_{cm} mean value of Nu in the zone of the substrate uniformly heated at the temperature T_v
Nu_m mean value of Nu on the whole substrate
P thermodynamic pressure [Pa or atm]
P_0 fluid thermodynamic pressure at static state [Pa or atm]
p differential motor pressure, $(P - P_0) + J\rho_0 g \int_0^z \rho_z(z)\,dz$ [Pa]
p_a 0, ambient motor pressure at the vertical level $z = 0$
p_i motor pressure at the nozzle entrance [Pa]
p_0 non-perturbed motor pressure in the interior of the nozzle [Pa]
Pr Prandtl number, $C_{p0}\mu_0/\lambda_0$
q local heat flux on the substrate [J m^{-2} s^{-1}]
R universal ideal gas constant, 8.3143435 J mole^{-1} K^{-1}
R_0 internal nozzle radius [m]
Re Reynolds number, $\rho_0 R_0 V_{max0}/\mu_0$
R_T radius of the total calculation domain [m]
R_1 radius of the domain uniformly heated to T_v, $10R_0$
R_2 radius where the substrate temperature reaches the room temperature, R_T
r radial direction space coordinate [m]
T temperature [K]
T_0 temperature at the nozzle entrance, here fixed at 298.15 K
T_v temperature on the substrate surface in the uniformly heated zone [K]
U mean velocity at the nozzle entrance, $\frac{1}{2}V_{max0}$ [m s^{-1}]
U_{max} maximal radial velocity defined in the whole calculation domain [m s^{-1}]
u radial velocity component [m s^{-1}]
V_{max0} maximal axial velocity at the nozzle entrance [m s^{-1}]
v axial velocity component [m s^{-1}]
z axial direction space coordinate [m].

Greek symbols
β pressure loss coefficient
Γ $\partial\Omega = \Sigma_i \Gamma_i$, boundary of the calculation domain
Γ_i boundary i of the calculation domain, $i = 1, 2, 3, \ldots, 7$
γ C_p/C_v
ΔT_0 characteristic temperature difference, $T_v - T_0$ [K]
ε Lennard–Jones potential characteristic energy [J]
θ non-dimensional temperature, $(T - T_0)/(T_v - T_0)$
θ azimuthal coordinate [radian]
λ thermal conductivity [J m^{-1} s^{-1} K^{-1}]
λ_0 λ value at the nozzle entrance [J m^{-1} s^{-1} K^{-1}]
μ dynamic viscosity [kg m^{-1} s^{-1}]
μ_0 μ value at the nozzle entrance [kg m^{-1} s^{-1}]
ρ density [kg m^{-3}]
ρ_0 ρ value at the nozzle entrance [kg m^{-3}]
$\rho_z(z)$ non-dimensional density on the boundary Γ_5, $= 1$
σ molecular hard-sphere diameter [Å (1 Å $= 10^{-10}$ m)]
ψ non-dimensional stream function, $d\psi = r^*\rho^* v^*\,dr^* - r^*\rho^* u^*\,dz^*$
ψ_0 value of ψ on the nozzle wall, 0.25.
ψ_{max} maximal stream function value in the whole plotted domain
ψ_{min} minimal stream function value in the whole plotted domain
Ω_c calculation domain, $R_T \times H_T$
Ω_s study domain, $10R_0 \times H$
Ω_r collision integral for the viscosity.

the case of confined jet reactor geometry. Wahl [14] used the finite difference method of secondary variables (stream-line function (ψ)–vorticity (ω) formulation) to solve the two-dimensional mathematical model in the case of a confined impinging jet configuration. The same problem was treated by Houtman *et al.* [15] by the finite elements method. As a result of their comparison between the one- and two-dimensional formulations, the one-dimensional model cannot account for the wall effects, nor buoyancy or finite susceptor radius.

In a non-confined configuration, Scholtz and Trass [16] studied theoretically and experimentally the impingement of an air jet on a flat plate for the non-uniform jet, that is, the fully developed parabolic velocity distribution at the nozzle entrance. For numerical purposes, the jet is divided into two regions: the bulk flow where the fluid is assumed to be inviscid but rotational, and the boundary layer near the wall. But the boundary layer theory failed to predict the non-monotonous radial variation of Sherwood number for cases of small nozzle–substrate distances, which is however experimentally measured, and justified later by our numerical results.

In a similar geometrical case, the flow field was studied numerically by Deshpande and Vaishnav [17] by the formulation of secondary variables (ψ–ω). The formulation of the boundary conditions is the main difficulty encountered with these variables, and particularly the vorticity on the solid walls or in the vicinity of the axis. At high Reynolds number their flow field is realistic, and our results are quite similar, but at low Reynolds number these authors have obtained a non-zero velocity on the nozzle exit wall which is inconsistent with the no-slip condition of a real fluid. The use of primary variables is not only much more straightforward, but also physically more meaningful.

More recently, Yuan *et al.* [18] modelled a two-dimensional laminar flow of a hot gas flowing on a cold surface from a slot exit. They used the finite-volume integration method developed by Patankar [19] assuming the Boussinesq approximation. Many authors [20–22] have discussed the application conditions of this approximation. They determined that it can only account for small temperature differences (<30 C). During the CVD process in a cold-wall reactor, the large temperature gradient is responsible for large variations of the physical properties, and that approximation is no longer valid. Then we have to take into account the dependence of physical properties on temperature, and possibly on pressure.

In the present study, a two-dimensional model with variable physical properties has been developed in the case of an axisymmetrical non-confined impinging jet under steady state conditions. Our attention was first focused on the determination of the flow profile under isothermal conditions. In the non-isothermal case, heat transfer rate was characterized for hydrogen gas as a function of the Reynolds and Froude numbers, substrate temperature, and nozzle–substrate distance. The gravity-induced buoyancy effects were investigated for different jet directions. In the last part, we compared the Nusselt number obtained from our numerical solution with the experimental data in the case of a small difference between the initial gas temperature and the substrate temperature.

MODEL DESCRIPTION

In our axisymmetrical vertical configuration, a jet emitted from a nozzle of radius R_0 impinges on a heated substrate at a distance H, in a semi-infinite medium (Fig. 1).

The continuity equation, the momentum equations in the r, z directions, and the energy balance equation are [23]:

$$\frac{1}{r}\frac{\partial}{\partial r}(r\rho u)+\frac{\partial}{\partial z}(\rho v)=0 \tag{1}$$

$$\frac{1}{r}\frac{\partial}{\partial r}(r\rho uu)+\frac{\partial}{\partial z}(\rho vu)=-\frac{\partial p}{\partial r}+\frac{1}{Re}\left\{\frac{1}{r}\frac{\partial}{\partial r}\left[r\mu\left(2\frac{\partial u}{\partial r}-\tfrac{2}{3}\nabla\cdot\mathbf{v}\right)\right]-\frac{\mu}{r}\left(2\frac{u}{r}-\tfrac{2}{3}\nabla\cdot\mathbf{v}\right)+\frac{\partial}{\partial z}\left[\mu\left(\frac{\partial v}{\partial r}+\frac{\partial u}{\partial z}\right)\right]\right\} \tag{2}$$

$$\frac{1}{r}\frac{\partial}{\partial r}(r\rho uv)+\frac{\partial}{\partial z}(\rho vv)=-\frac{\partial p}{\partial z}+\frac{1}{Re}\left\{\frac{1}{r}\frac{\partial}{\partial r}\left[r\mu\left(\frac{\partial v}{\partial r}+\frac{\partial u}{\partial z}\right)\right]+\frac{\partial}{\partial z}\left[\mu\left(2\frac{\partial v}{\partial z}-\tfrac{2}{3}\nabla\cdot\mathbf{v}\right)\right]\right\}-J\frac{\rho-\rho_z(z)}{Fr} \tag{3}$$

$$\frac{1}{r}\frac{\partial}{\partial r}[(r\rho u)C_p\theta]+\frac{\partial}{\partial z}[(\rho v)C_p\theta]=\frac{1}{Re\,Pr}\left\{\frac{1}{r}\frac{\partial}{\partial r}\left(r\lambda\frac{\partial\theta}{\partial r}\right)+\frac{\partial}{\partial z}\left(\lambda\frac{\partial\theta}{\partial z}\right)\right\} \tag{4}$$

with the velocity divergence:

$$\nabla\cdot\mathbf{v}=\frac{1}{r}\frac{\partial}{\partial r}(ru)+\frac{\partial v}{\partial z}. \tag{5}$$

Non-dimensional variables are used, but, for a matter of simplicity, the conventional non-dimensional symbol '*' is not mentioned. The reference values for the non-dimensional variables are: R_0, V_{max0}, ρ_0, C_{p0}, μ_0, λ_0 and ΔT_0 (difference between room and substrate temperature). Nevertheless, discussion of the results will refer to dimensional variables in order to improve our understanding of the physical phenomena.

The classical following hypotheses have been assumed. The axisymmetrical reactor is two-dimensional, so that the azimuthal velocity component is zero. The steady state flow is laminar, and the gas has a Newtonian behaviour. Due to the very low Mach

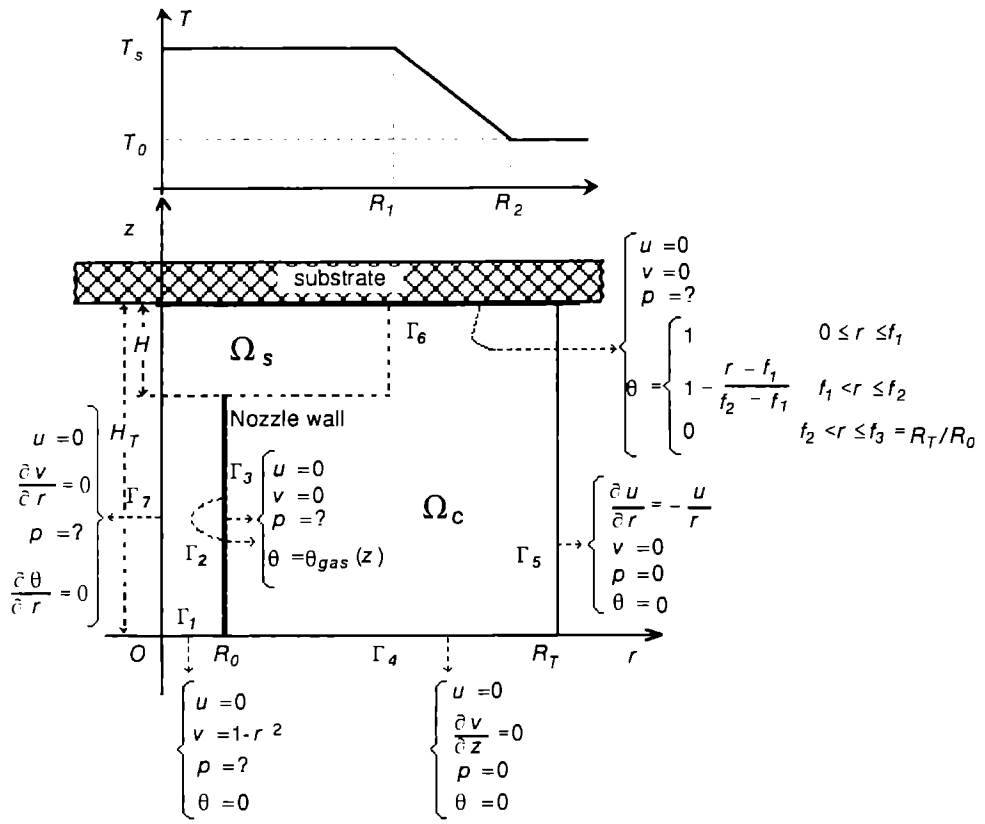

FIG. 1. Schematic diagram of the reactor, including calculation domains, boundary conditions, and the temperature distribution along the substrate surface.

number the gas is supposed to be incompressible. Heat variations resulting from compression, viscous dissipation, or radiation are neglected in the heat balance.

Figure 1 presents the boundary conditions. Because of the non-confined geometry, two kinds of boundary conditions are expected: classical boundary conditions are defined on surfaces Γ_1, Γ_2, Γ_3, Γ_6 and Γ_7, though the true behaviour corresponding to zero velocity is only known at infinity for the free boundaries Γ_4 and Γ_5.

On Γ_1, the gas is assumed to be at room temperature T_0, and the Hagen–Poiseuille flow conditions are assumed, that is to say the fully developed flow with parabolic axial velocity distribution and zero radial velocity is settled.

On Γ_2 and Γ_3, which are the internal and external walls of the nozzle, a no slip condition is assumed for the velocity field. Moreover, due to the perfect heat conduction through the infinitely thin walls of the nozzle, the temperature of the neighbouring gas is the same on both sides.

On Γ_6 which is the surface of the substrate, the temperature T_s is constant in a disk domain of radius R_1, and decreases linearly until the radius R_2 where it reaches the room temperature (Fig. 1).

On Γ_7, which is the axis, the boundary conditions are imposed on grounds of symmetry.

The pressure level in the whole domain is determined by the zero driving pressure on the free boundaries Γ_4 and Γ_5.

With a finite calculation domain as shown in Fig. 1, the boundary conditions on Γ_4 and Γ_5 are the most debatable. Yuan *et al.* as well as Mikhail *et al.* [24] used the zero variation condition for both velocity components, that is, $\partial u/\partial n = \partial v/\partial n = 0$. These conditions do not meet the local continuity equation requirements, and an imbalance of the mass flow rate is generated. In our case, the zero tangential velocity and the zero variation of the normal velocity are imposed on Γ_4. On Γ_5, the tangential velocity is zero, and the normal velocity component is deduced from the continuity equation, therefore the global mass balance complies with these conditions.

For a non-compressible Newtonian fluid, the physical properties ρ, C_p, μ, λ are only dependent on temperature. Their temperature dependence was calculated according to references [25–27] from the following equations

$$\rho = \frac{P_0 M}{RT} \tag{6}$$

$$C_p = A + BT + CT^2 + DT^3 \quad (7)$$

$$\mu = 26.69 \times 10^{-7} \frac{\sqrt{MT}}{\sigma^2 \Omega_\mu} \quad (8)$$

$$\lambda = \left(\frac{1.473 \times 10^{-4}}{M} + \frac{1.32}{\gamma} C_p\right)\mu. \quad (9)$$

The ideal gas state equation is used to obtain the density; the specific heat C_p is modellized by a 3-degree polynomial expression; the Chapman–Enskog treatment based on the Lennard–Jones potential parameters is used for the viscosity, and the thermal conductivity is obtained from the modified Eucken equation.

NUMERICAL METHOD

Numerical integration of the partial differential equations on an elementary volume formed by mesh

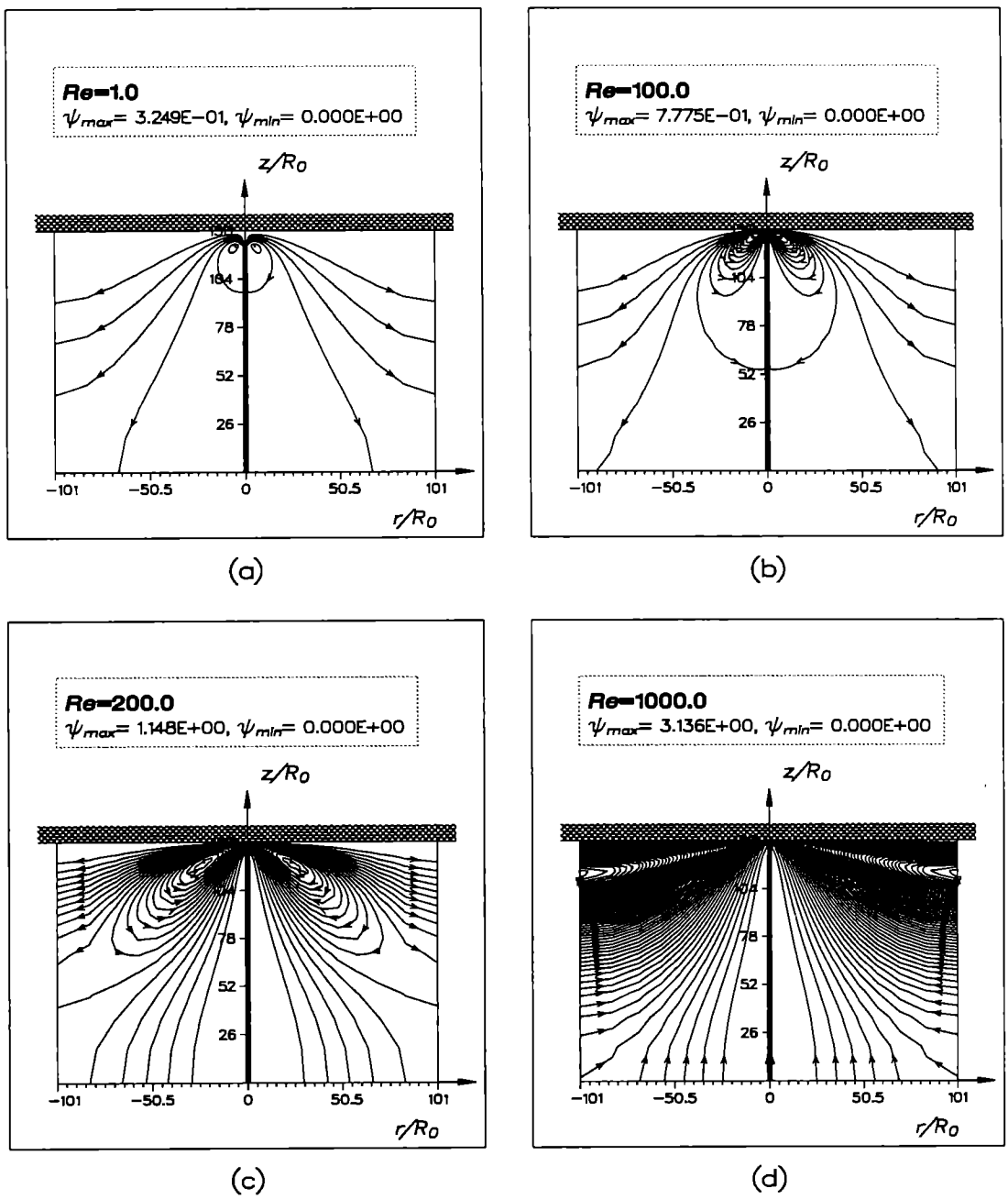

FIG. 2. Streamlines for different Reynolds numbers, in isothermal case ($H/R_0 = 8$).

Table 1. Maximal radial velocity and its location in the whole calculation domain for $Re = 100$ and $H/R_0 = 8$

No. calculation	Calculation domain sizes Ω_c	Mesh grids M	Boundary conditions Γ_4	Boundary conditions Γ_5	U_{max}/V_{max0}	Location of U_{max} r/R_0	h/R_0	ψ_{max}
1	$21R_0 \times 28R_0$	31×31	$u = 0$, $\partial v/\partial z = 0$	$(\partial u/\partial r) = -(u/r)$, $v = 0$	0.2565	1.442	0.3112	0.8195
2	$31R_0 \times 38R_0$	Idem to No. 1	Idem to No. 1	Idem to No. 1	0.2564	1.453	0.3112	0.8093
3	$41R_0 \times 48R_0$	Idem to No. 1	Idem to No. 1	Idem to No. 1	0.2563	1.461	0.3112	0.8007
4	$101R_0 \times 130R_0$	Idem to No. 1	Idem to No. 1	Idem to No. 1	0.2561	1.486	0.3112	0.7930
5	$21R_0 \times 28R_0$	41×41	Idem to No. 1	Idem to No. 1	0.2565	1.422	0.3112	0.8318
6	$21R_0 \times 28R_0$	Idem to No. 1	$u = 0$, $r = 0$	Idem to No. 1	0.2565	1.442	0.3112	0.8175
7	$21R_0 \times 28R_0$	Idem to No. 1	Idem to No. 1	$\partial u/\partial r = 0$, $r = 0$	0.2565	1.442	0.3112	0.8192

grids was performed by the finite-volume technique developed by Patankar [19]. The scalar variables such as temperature or pressure were solved at the centre of the volume, whereas the components of the vectorial variables (velocity), were solved at the centre of the face of the volume. Evolutive steps were adopted for the mesh grid in both radial and axial directions with the finer mesh near the boundaries Γ_6 and Γ_7.

This discretization method led to a linear algebraic equation system which was then solved by the algorithm SIMPLER (Semi-Implicit Method for Pressure-Linked Equation Revised) [19]. This iterative method consists in solving the linear algebraic equation system for each variable separately. The pressure was deduced from the velocity field according to the continuity equation so that the velocity complies with the mass continuity.

The set of linear equations was solved by the TDMA (Tri-Diagonal Matrix Algorithm) line by line method, or by a sparse matrix technique. The iteration ended when the relative error of two consecutive values for each variable at each node was less than 0.1% and when the balance of the flow rate in any finite-volume did not exceed 0.1%. As a consequence the total flow rate balance was satisfied with a relative error of less than 10^{-4}% of the flow rate at the nozzle entrance. The program was performed on a micro DEC VAC 3600 machine (ratio = 30, or 30 times slower than CRAY-1S) in Fortran language. For a mesh grid of 31×31 points, an isothermal calculation lasted about 15 min CPU time, and a non-isothermal problem required 1 h or more.

RESULTS

We first looked at the influence of the boundary conditions on Γ_4 and Γ_5, at the influence of the size of the calculation domain Ω_c, and at the influence of

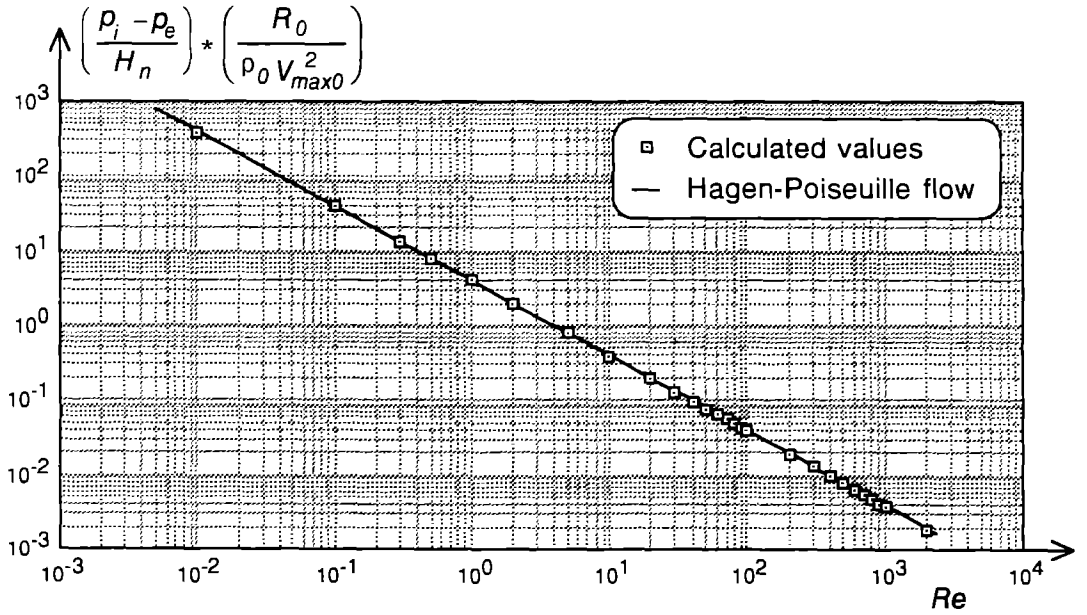

FIG. 3. Viscous pressure loss between the nozzle entrance and exit along the Oz axis, $H/R_0 = 8$.

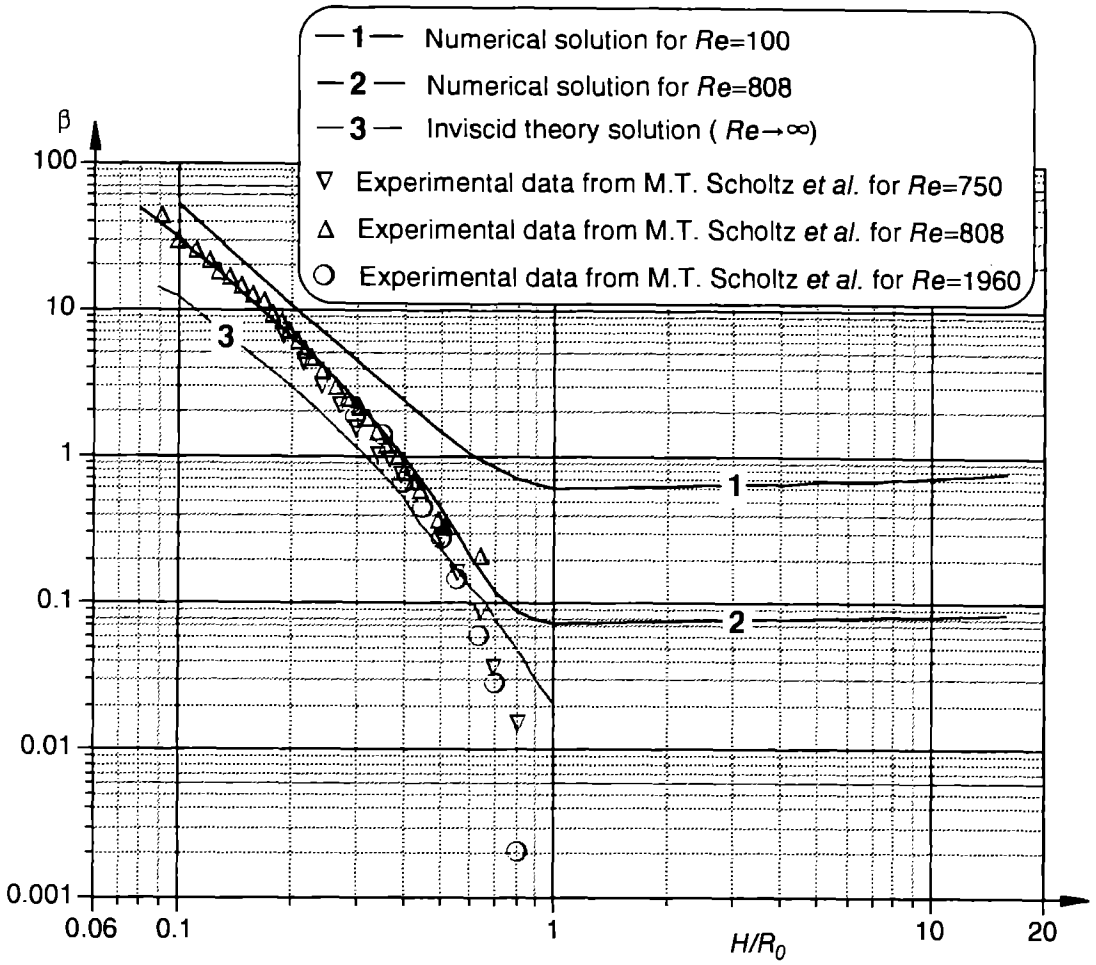

FIG. 4. Pressure loss coefficients.

the mesh grids, on the results of the calculation for the following conditions: $Re = 100$, $H/R_0 = 8$. The selected criteria were the maximum radial velocity U_{max} and its location, the maximum non-dimensional stream function ψ_{max} which characterizes the entrained flow rate, as well as the flow pattern in the domain Ω_s. This domain is a cylindrical zone ($10R_0 \times H$) near the substrate (Fig. 1) which is the most important domain from a CVD point of view. According to these criteria and the absence of significant difference in the flow fields calculated in domain Ω_s, the various calculation conditions were equivalent (Table 1). As a consequence, further calculations were performed in the smallest calculation domain ($21R_0 \times 28R_0$) with a 31×31 points mesh grid, and for the boundary conditions on Γ_4, Γ_5 shown in Fig. 1.

Isothermal flow

The calculation was first undertaken for isothermal conditions and the results compared with experimental measurements from the literature.

For a nozzle–substrate distance $H/R_0 = 8$, the influence of the Reynolds number was investigated in the range 0.01–2000. Typical velocity fields characterized by the stream lines are shown in Fig. 2 for $Re = 1$, 100, 200 and 1000. A toroidal recirculation cell is observed at low Reynolds number around the nozzle exit. Its diameter increases with Re in accordance with Scholtz's observations.

A more quantitative result is the viscous pressure loss occurring between entrance and exit of the nozzle. Figure 3 shows the good agreement between our numerical solution and that calculated with the Hagen–Poiseuille theory for a fully developed laminar flow in a cylindrical tube. A slight deviation which increases with Re, reaches a maximum departure of 8% for $Re = 2000$. This results from the evolution along the nozzle of the initially zero radial velocity, which modifies the fully developed flow.

The pressure loss coefficient β, which represents the pressure variation due to constriction of the flow in terms of the kinetic energy in the nozzle as defined by Scholtz, was also calculated:

$$\beta = \frac{p_n - p_a}{\rho_0 U^2}. \tag{10}$$

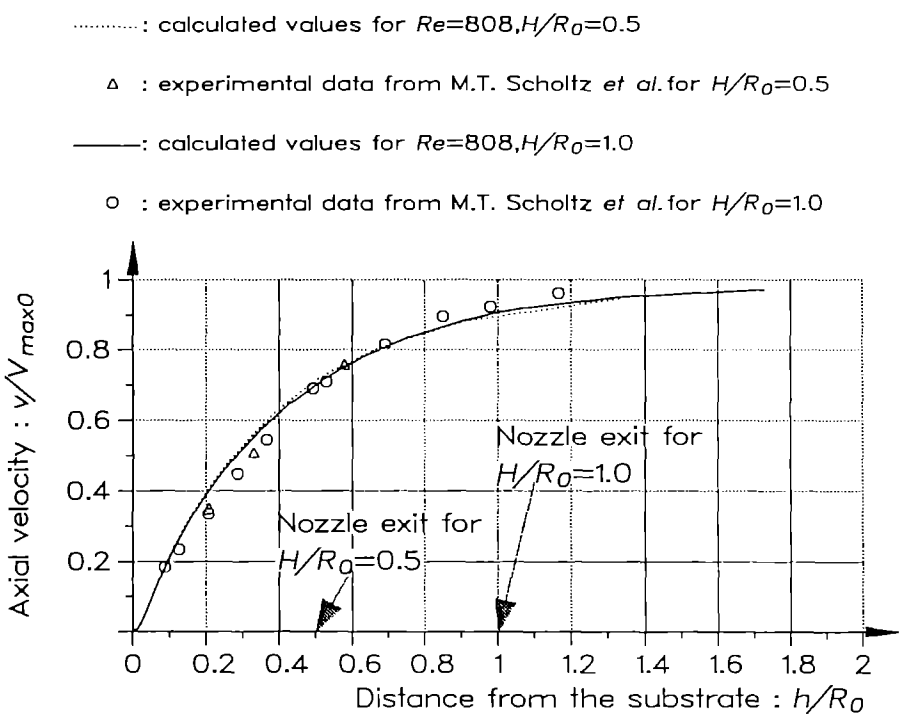

FIG. 5. Variation of axial velocity with distance from the substrate on axis Oz, comparison between experimental data and calculated values.

In order to compare our numerical results with Scholtz's measurements, the p_n values were calculated in the nozzle at the same distance from the nozzle exit ($4R_0$). For $Re = 808$, the data measured by Scholtz (triangles pointed upwards) are compared in Fig. 4 with our numerical solution for the same conditions (curve 2) and reveal a very satisfactory agreement. The slight discrepancy between the inviscid solution calculated by the same author (curve 3) and the measurements obviously results from the omitted viscous dissipation. The calculated β are greater for $Re = 100$ (curve 1) than for $Re = 808$ (curve 2) on account of the more important viscous dissipation. The experimental data for $Re = 750$ (triangles pointed downwards) and for $Re = 1960$ (circles) furthermore reveal the independence of the pressure loss coefficient on the Reynolds number.

The axial velocity measured out of the nozzle by Scholtz is also compared with our calculation for two nozzle–surface distance in Fig. 5 and reveals once more a quite good agreement.

The validity of our numerical model is confirmed in the isothermal case, and we will now consider the non-isothermal flow for the conditions that prevail in the CVD process.

Non-isothermal flow

As the dependence of the physical properties on temperature is specific to the gas used, this has to be specified in the non-isothermal case. Hydrogen is frequently used as a carrier gas, and reducing agent for CVD applications and will be considered in all further calculations.

We have undertaken a systematic investigation of the influence of various parameters on heat transfer. Reference conditions with the following values, have been defined as a comparison: $P_0 = 1$ atm, $T_0 = 298.15$ K, $T_s = 1333.15$ K, $V_{max0} = 1$ m s^{-1}, $R_0 = 0.01$ m, $H = 0.08$ m, and the corresponding non-dimensional parameters: $Re = 93.13$, $Fr = 10.20$, $Pr = 0.6904$.

The heat transfer rate has been characterized by the local Nusselt number:

$$Nu = \frac{k_H R_0}{\lambda_0} \tag{11}$$

with the heat flux:

$$q = k_H \Delta T_0 = k_H (T_s - T_0). \tag{12}$$

As already mentioned, the use of the Boussinesq approximation is not correct in the case of large temperature gradients. This is illustrated in Fig. 6 for various dependence models of the physical properties of the fluid on temperature. This figure compares the variation of the local Nusselt number, which is calculated according to the variable physical properties model, with that assuming the Boussinesq approximation in both cases of mean physical properties in all the calculation domain and physical properties calculated at the mean temperature. The domain of

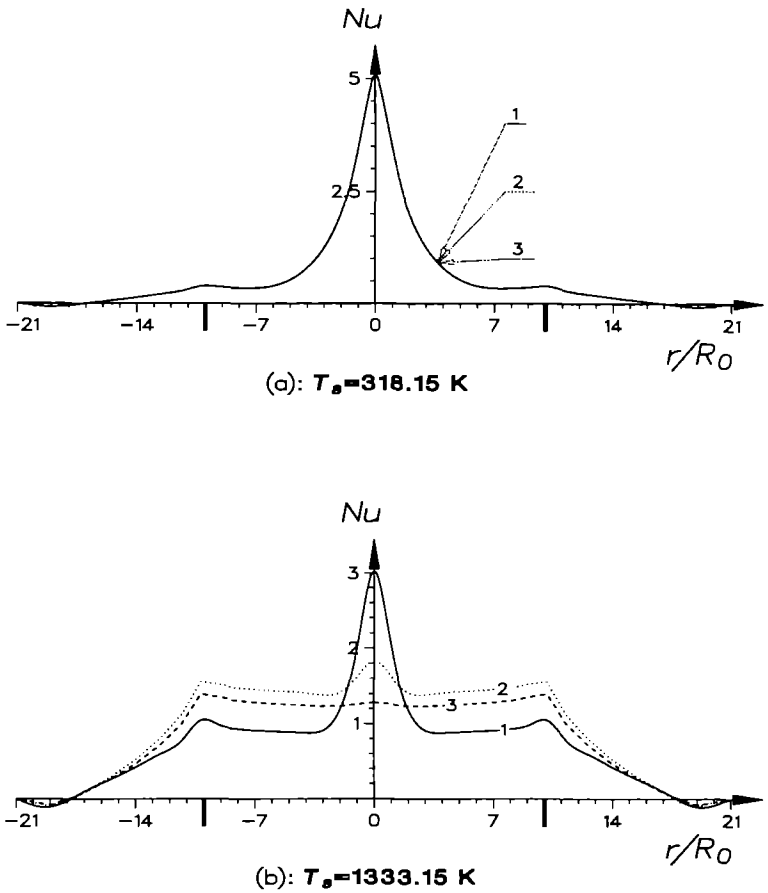

FIG. 6. Variation of local Nusselt number according to the model used. $J = 1$, $Re = 93.13$, $Fr = 10.20$, $Pr = 0.6904$, $T_0 = 298.15$ K, $H/R_0 = 8.0$. 1 : variable properties model ; 2 : Boussinesq approximation with mean property values ; 3 : Boussinesq approximation with property values at mean temperature.

uniform T_s temperature is limited by two bold ticks on the radial axis at $-10R_0$ and $10R_0$.

At high temperature (T_s at 1333.15 K, $\Delta T_0 = 1035$ K), it is obvious from curves 1, 2 and 3 of Fig. 6(b) that the Boussinesq approximation underestimates the Nusselt number in the central zone in front of the nozzle exit, whereas the transfer rate is over-estimated beyond that domain.

At low temperature (T_s at 318.15 K, $\Delta T_0 = 20$ K), in Fig. 6(a), the three methods of evaluation of physical properties give almost the same Nusselt number value over the whole calculated domain. The relative error on Nu_0 values, lower than 1% vindicates the Boussinesq approximation in the case of a small temperature gradient.

All further calculations will be carried out with the variable properties model. Let us now look at the variation of the Nusselt number according to various parameters. Only one parameter is modified at a time, all other parameters are in their reference state.

Reynolds number and Nusselt number. As expected the heat transfer is enhanced at high flow rate (Fig. 7). For the same conditions, the mean Nusselt number on the central zone uniformly heated at T_s (Nu_{cm}), and the mean Nusselt number on the whole surface (Nu_m) are also plotted.

The normalized Nusselt number (Nu/Nu_0) plotted against r/R_0 in Fig. 7(b) reveals that heat transfer is maximum on the axis of the impinging jet only for Reynolds numbers higher than 10. At very low flow-rates, an annular maximum is observed at the boundary of the isothermal domain. In this latter case the natural convection is preponderant and its influence is more important at the periphery.

At high flow rates the fluid flow is maximum in front of the nozzle where it involves the highest heat transfer. It is worth noting that the Nusselt number is almost constant in the isothermal zone of the substrate for Re values close to 10.

Froude number and Nusselt number. The Froude number is the ratio of the inertial force to the gravitational force. The relative importance of the natural convection compared with the forced convection is classically estimated by $G = Gr/Re^2$ (Gr is the Grashof number), which is a function of the Froude number (Fr) :

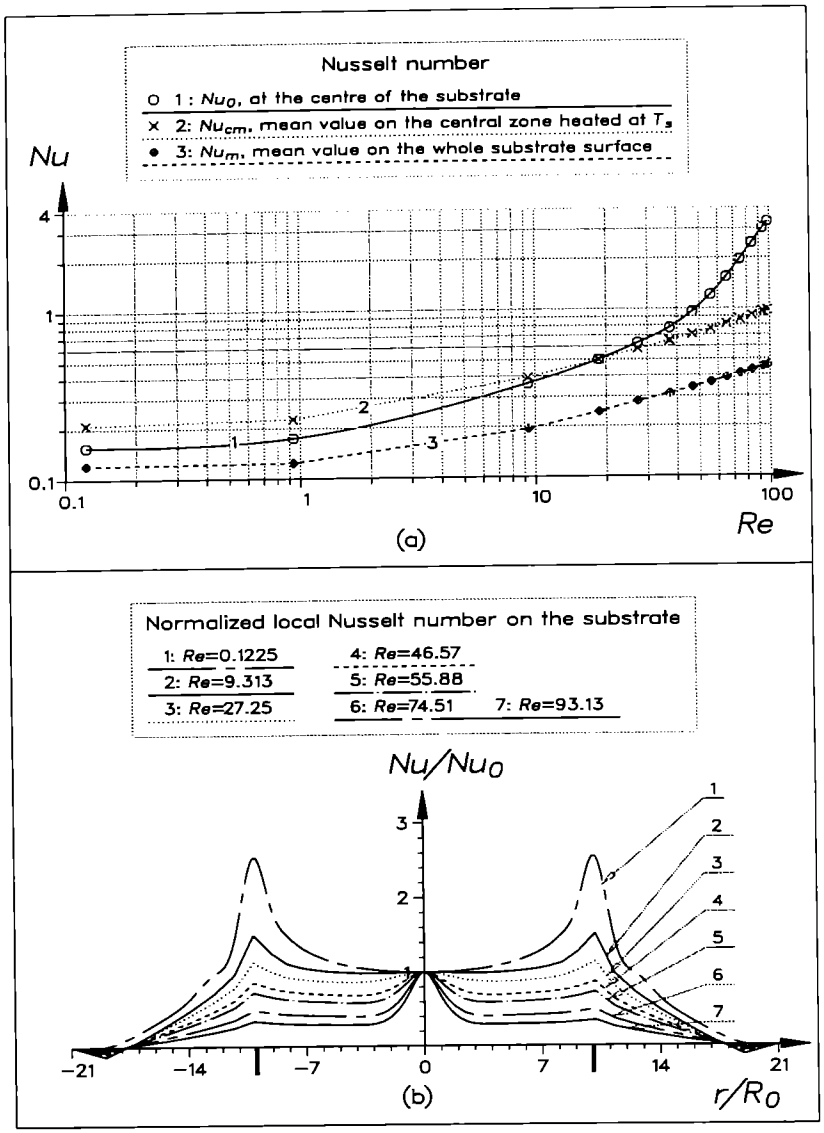

FIG. 7. Evolution of Nusselt number as a function of Re. (a) Nu_0, Nu_{cm}, Nu_m; (b) Nu/Nu_0: normalized local Nusselt number; $J = 1$, $Fr = 10.20$, $Pr = 0.6904$, $T_0 = 298.15$ K, $T_s = 1333.15$ K, $H/R_0 = 8.0$.

$$G = \frac{1}{Fr}\frac{T_s - T_0}{T_0}. \tag{13}$$

The maximum observed for the variation of Nu_0 plotted against G in Fig. 8(a) may be explained in the following way. As the jet is flowing upwards, both natural and forced convection act in the same direction. For the low G values, which correspond to the predominant forced convection, the relative increase of the natural convection reinforces the flow rate along the nozzle axis and enhances Nu_0. When the natural convection is predominant (see Fig. 12(b)) for pure natural convection fluid flow) its influence is very strong at the periphery of the jet and prevents the fluid leaving the nozzle from expanding freely. In this case natural convection reduces the flow rate along the nozzle axis and Nu_0 decreases with G. Far from the nozzle axis no maximum is observed and Nu increases continuously with G (Fig. 8(b)) because of the increasing entrainment of the cold gases with natural convection.

In a confined configuration the critical value (G_0) determined by Wahl [14] was unity, though $G_0 \approx 2 \times 10^{-2}$ is found in our case.

Nozzle–substrate distance and Nusselt number. As expected, when the nozzle is moved away from the surface, the heat transfer at the stagnation point decreases regularly because of the spreading effect of the jet (Fig. 9(a)).

The shape of the normalized Nusselt number along

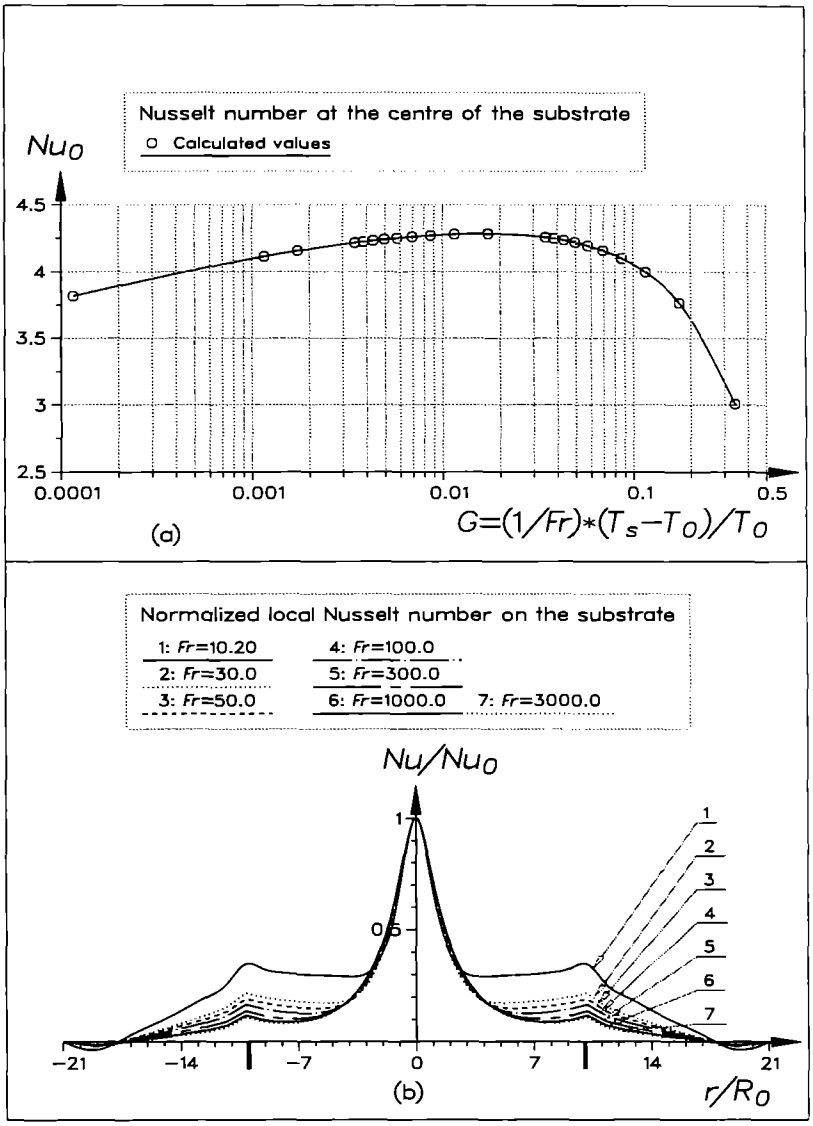

FIG. 8. Evolution of Nusselt number as a function of Fr. (a) Nu_0: Nusselt number at the centre of the substrate; (b) Nu/Nu_0: normalized local Nusselt number: $J = 1$, $Re = 93.13$, $Pr = 0.6904$, $T_0 = 298.15$ K, $T_s = 1333.15$ K, $H/R_0 = 8.0$.

the substrate is slightly dependent on the nozzle–substrate distance when H/R_0 is greater than unity (Fig. 9(b)). On the contrary, a strong influence is observed when the nozzle is very close to the surface. Then, the crushing of the jet through the narrow space between nozzle and substrate is locally responsible for a great radial velocity, thus providing a maximal heat transfer located at the radius of the nozzle R_0 (curve 1, Fig. 9(b)).

Substrate temperature and Nusselt number. The combined influence of the temperature dependence of the physical properties and natural convection tends to reduce the Nusselt number at the stagnation point at high temperature (Fig. 10(a)). At the same time, the relative influence of heat transfer off the axis is enhanced (Fig. 10(b)). The annular maximum already observed at the boundary of the isothermal domain when looking at the influence of the Reynolds number, is also induced in that case by natural convection.

Jet direction and Nusselt number. Upward and downward vertical jets have been respectively investigated to determine the effects of the gravitationally-induced fluid flow modifications.

The various behaviours of the local Nusselt number presented in Fig. 11 correspond to different values of the J parameter which indicates the jet direction: $J = 1$ for the upward jet, $J = -1$ for the downward jet and $J = 0$ for a hypothetical case with no terrestrial gravity. In addition, the fluid flow driven by pure

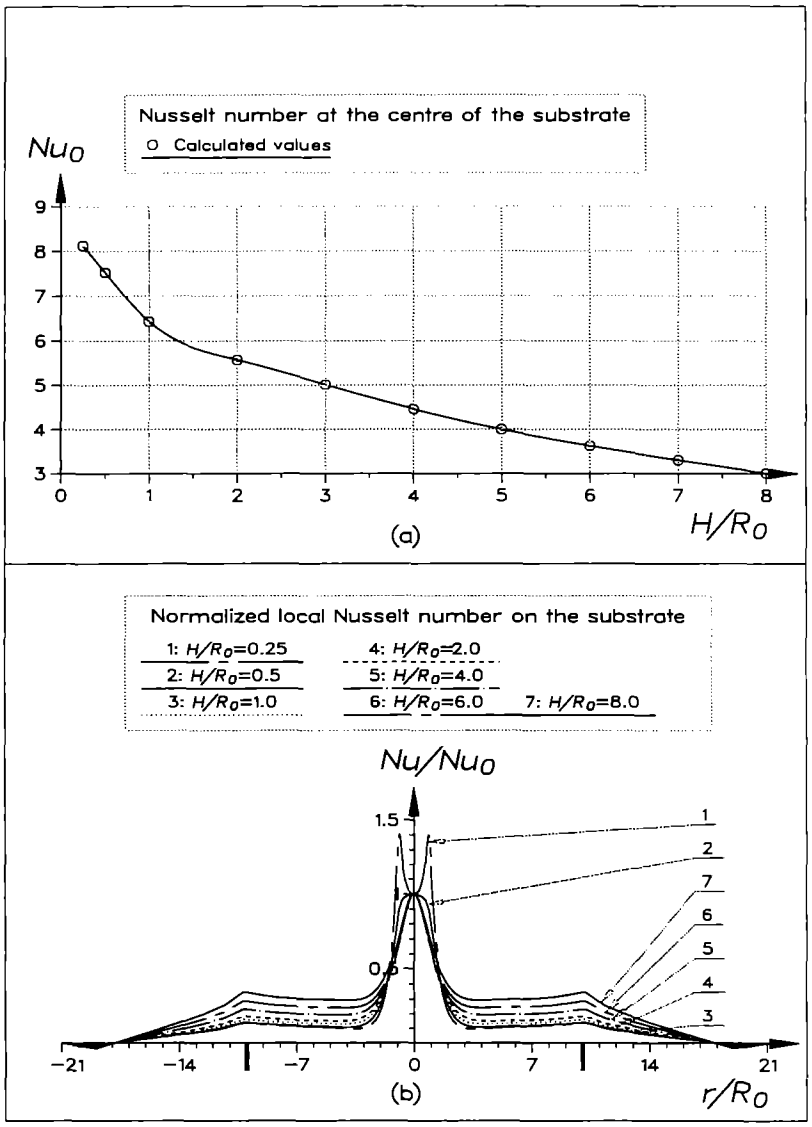

FIG. 9. Evolution of Nusselt number as a function of H/R_0. (a) Nu_0: Nusselt number at the centre of the substrate; (b) Nu/Nu_0: normalized local Nusselt number; $J = 1$, $Re = 93.13$, $Fr = 10.20$, $Pr = 0.6904$, $T_0 = 298.15$ K, $T_s = 1333.15$ K.

natural convection (zero velocity at the entrance of the nozzle) is also considered for the upward situation. This allows us to distinguish between the influence of the impinging flow and that of natural convection. The zone where curves 2 and 3 are superposed in the peripheral part of the jet defines the domain of preponderant natural convection. In the central zone, the impinging flow accounts for the large variation observed for Nu_0 in the two cases: 0.85 vs 3.0. The heat transfer is only reinforced in the impinging zone by the jet, no influence is observed in the remote zone ($r/R_0 > 3$), where heat transfer is almost completely controlled by natural convection.

From the comparison of curves 3 and 1, or 4 and 1, the maximum heat transfer in the vicinity of the stagnation point is obviously reached in the absence of gravity influence. The negative effect of gravity on Nusselt number for the downward jet is conspicuous, since the induced natural convection is in the opposite direction of the jet, but the upward situation is not so straightforward and two cases are observed. As already discussed, natural convection improves the heat transfer at the stagnation point only for $G < G_0$. For the calculated conditions mentioned in Fig. 11 the ΔT_0 value corresponding to the transition ($G_0 = 10^{-2}$) is 30 K. According to this very small difference, the gravity field reduces the heat transfer at the stagnation point in almost all cases and an accurate representation of the curve shown in Fig. 10(a) should display a small domain at $T_s < 328$ K where Nu_0 increases with T_s.

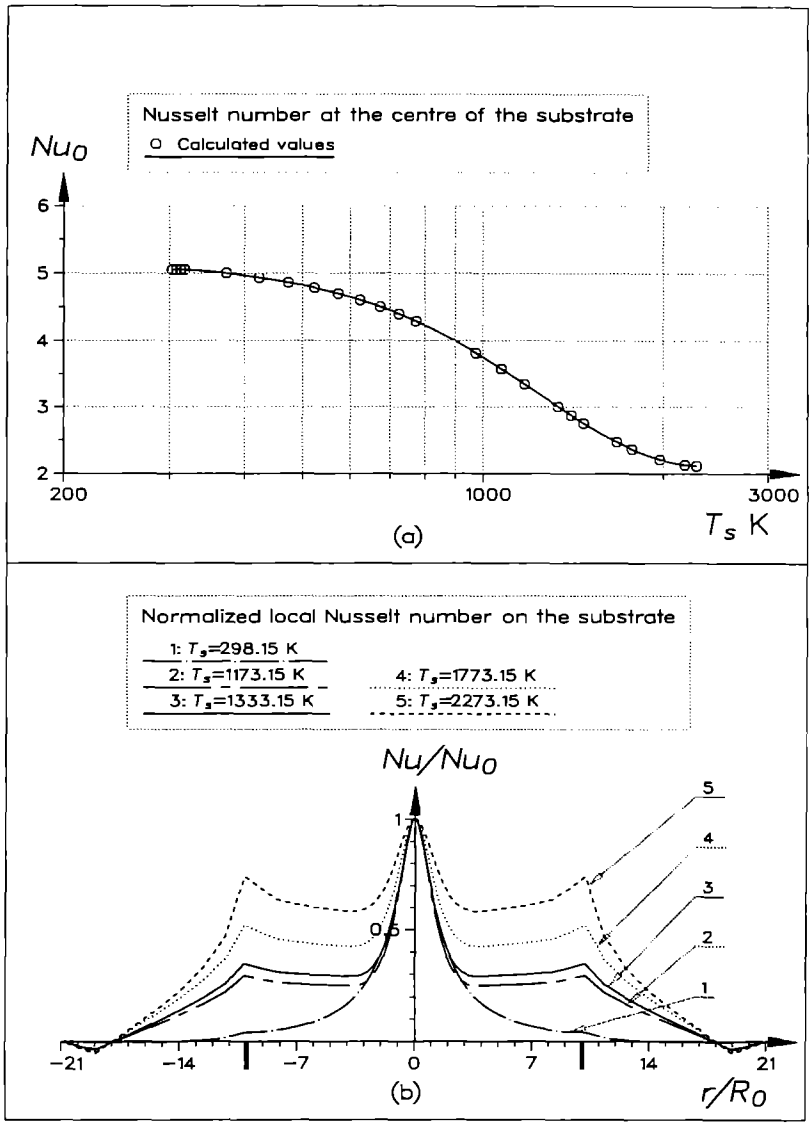

FIG. 10. Evolution of Nusselt number as a function of T_s. (a) Nu_0: Nusselt number at the centre of the substrate; (b) Nu/Nu_0: normalized local Nusselt number; $J = 1$, $Re = 93.13$, $Fr = 10.20$, $Pr = 0.6904$, $T_0 = 298.15$ K, $H/R_0 = 8.0$.

Stream lines (right hand side) and isotherms (left hand side) are shown in Fig. 12 for the four cases discussed above. The two basic cases corresponding to pure forced convection and pure natural convection are presented respectively in Figs. 12(a) and (b). In case (a) the fluid leaving the nozzle flows first towards the stagnation point and then along the substrate. In the latter case, the variation of the momentum thickness is that expected from a flow past a flat plate at zero incidence. On the other hand, in pure natural convection situation shown in Fig. 12(b), a very strong buoyancy-driven flow is observed. This phenomena is maximum at the boundary of the calculation domain. The high number of close streamlines in the buoyancy-driven flow shows that it is much more important than the forced flow and limits the expansion of the thermal boundary layer.

As a consequence of these two convection sources, the behaviour of the upward jet in the gravity field (Fig. 12(c)) looks like the superposition of the two sets of stream lines. As already mentioned, the buoyancy driven flow is very strong at the periphery of the jet and prevents the fluid leaving the nozzle from expanding freely.

The last case in Fig. 12(d) illustrates a completely different shape of the velocity field related to the downward jet. On the right hand side of the figure, one observes that the downward movement of the fluid is annihilated so rapidly by the upward buoyancy-driven flow facing upwards, that the fluid pro-

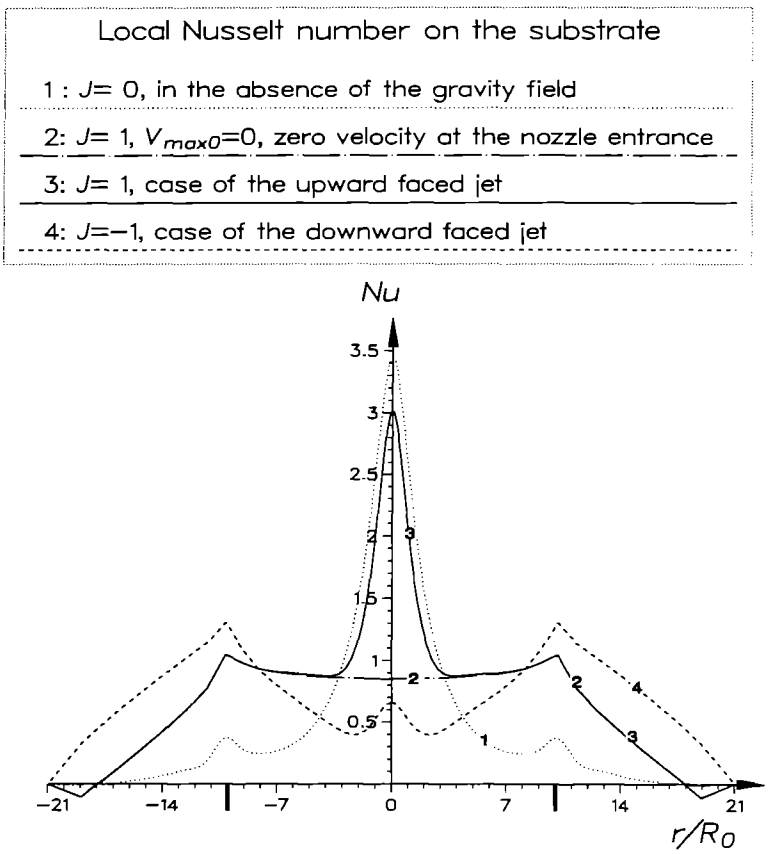

FIG. 11. Evolution of Nusselt number as function of J. Calculation conditions: for the cases 1, 3, 4: $Re = 93.13$, $Fr = 10.20$; for the cases 1, 2, 3, 4: $Pr = 0.6904$, $T_0 = 298.15$ K, $T_s = 1333.15$ K, $H/R_0 = 8.0$.

jected does not effectively reach the surface of the substrate. This explains *a posteriori* why the heat transfer is disfavoured in the impinging zone in the case of the downward jet when compared with the upward jet.

Though obtained under different conditions, these results are quite comparable with that of Yuan *et al.* [18].

Experimental validation. Due to the lack of heat transfer measurements available in the literature for the laminar jet, we used an indirect method which consists in converting the mass transfer data (Sherwood number) into Nusselt number by the Chilton–Colburn analogy [23]. In addition to the standard correlation $Nu/Sh = (Pr/Sc)^{1/3}$ a modification is often encountered in the literature: $Nu/Sh = (Pr/Sc)^{0.4}$. As they both provided similar results in our case, the last one was arbitrarily chosen. The numerical solution was calculated for hydrogen gas at 25°C under 1 atm ($Pr = 0.6904$). The experimental mass transfer data came from Scholtz and Trass [16], who measured the local sublimation rates of a naphthalene coating exposed to an air jet at room temperature. For a small difference between the initial gas temperature and the substrate temperature, the physical properties of the gas are assumed to be constant and the Nusselt number is independent of the chemical nature of the gas.

A critical dimensionless nozzle–substrate distance of 0.25 was determined both from our calculation and from Scholtz's experiments. Two types of Nusselt number profiles were then observed. When the nozzle–substrate distance is greater than the critical value, the Nusselt number decreases monotonously with the radial distance from the maximum value located at the centre of the substrate surface (Fig. 13).

On the other hand, when a very small nozzle–substrate distance is used ($H/R_0 \leqslant 0.25$), the Nusselt number variation is no longer monotonous, and the maximum value is found at a distance corresponding to the nozzle radius (Fig. 14).

The calculated and experimental Nusselt number profiles are compared in Fig. 13 for a nozzle–substrate distance $H/R_0 = 1$. The agreement between the experimental data for $Re = 375$ and the calculated values in the same conditions (curve 2) is quite good up to large dimensionless radial distance.

In order to show the influence of the Reynolds number, the Nusselt number profile was calculated for $Re = 100$ (curve 1) and $Re = 2000$ (curve 3). The superposition of curves 2 and 3 observed for radial distance r/R_0 ranging from 0 to 1 confirms the dependence: $Nu = f(Re^{0.5})$ obtained by the analytical solution when neglecting both the natural convection, and the viscous contribution for the bulk flow. This depend-

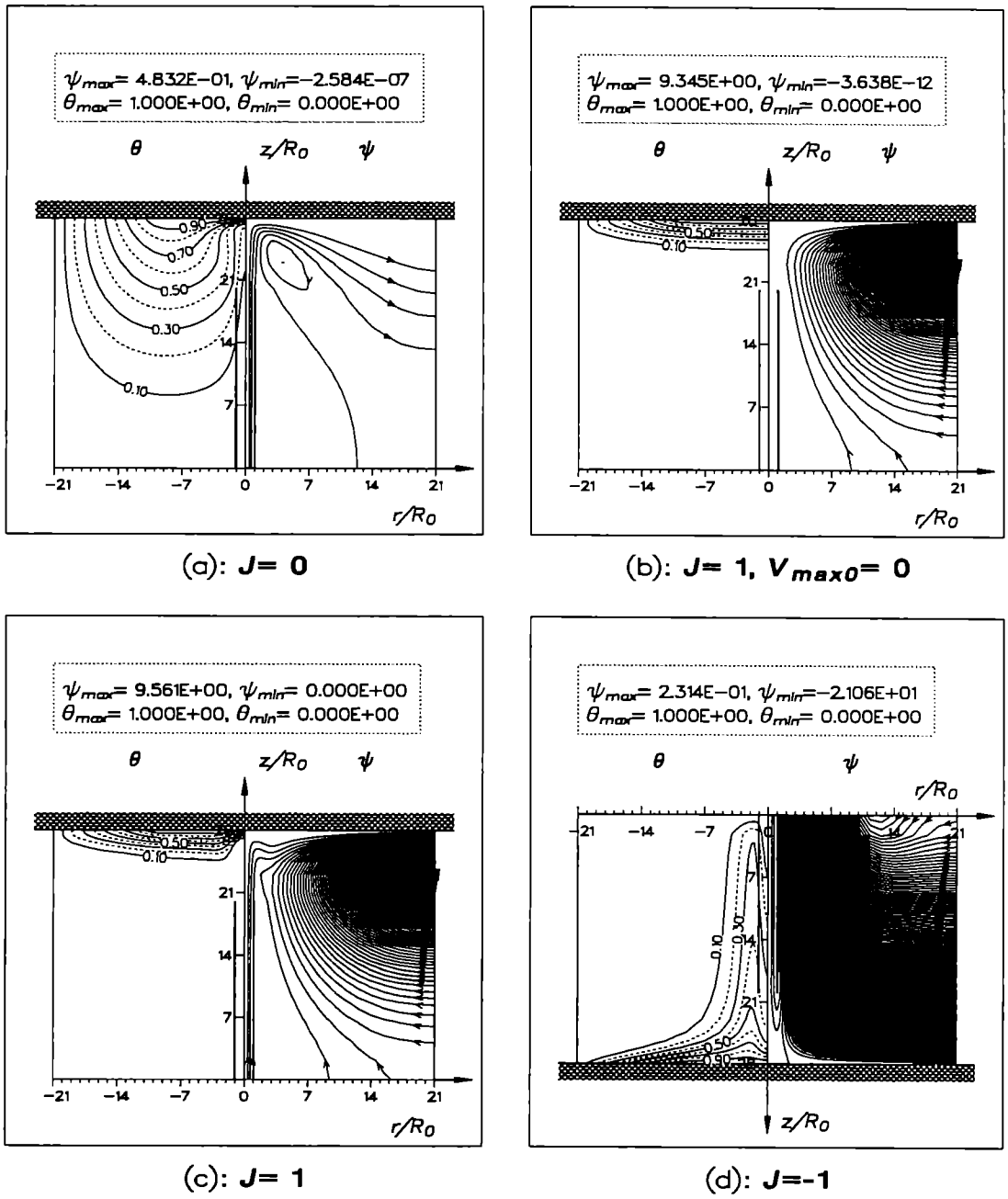

FIG. 12. Streamlines (right hand side) and isotherms (left hand side). $R_0 = 0.01$ m, $H/R_0 = 8.0$, $T_0 = 298.15$ K, $T_s = 1333.15$ K, $P_0 = 1.0$ atm, and $V_{max0} = 1.0$ m s^{-1} for the cases a, c and d. (a) $J = 0$, in the absence of the gravity field; (b) $J = 0$ and $V_{max0} = 0$, null velocity at the nozzle entrance; (c) $J = 1$, case of the upward facing jet; (d) $J = 0$, case of the downward facing jet.

ence accounts only for small differences of temperature, high Reynolds number, pure forced convection, and inviscid fluids. When the temperature difference is large and the Reynolds number is low, a more complicated variation of the Nusselt number as a function of the Reynolds number is observed because of the large influence of natural convection (Fig. 7(a)). A large departure from the high Reynolds number case (curves 2, 3) is then observed even with a small temperature difference (curve 1).

When the dimensionless nozzle–substrate distance is greater than 1, its influence on the Nusselt number is small (curve 4: $H/R_0 = 8$, $Re = 800$).

Due to the similarity of the $Nu/(Re^{0.5}\,Pr^{0.4})$ profile

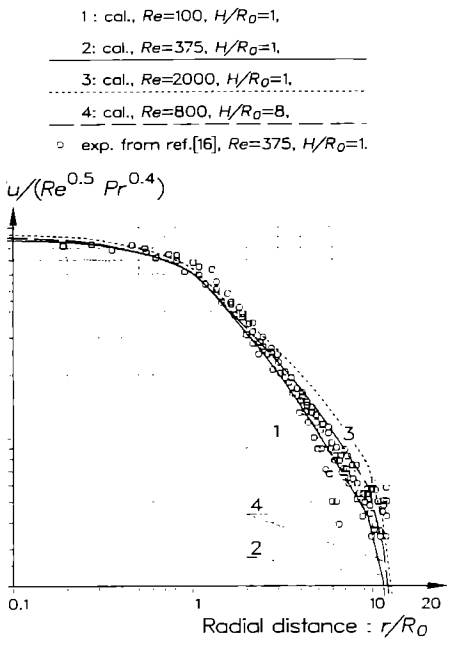

FIG. 13. Local Nusselt number profile on the substrate surface, comparison of the calculated values with experimental data, $Pr = 0.6904$ and $H/R_0 = 1.0$ except for the curve 4.

observed for various Reynolds and Prandtl numbers, the local Nusselt number can be described as a function of the dimensionless radial distance by the following polynomial equation:

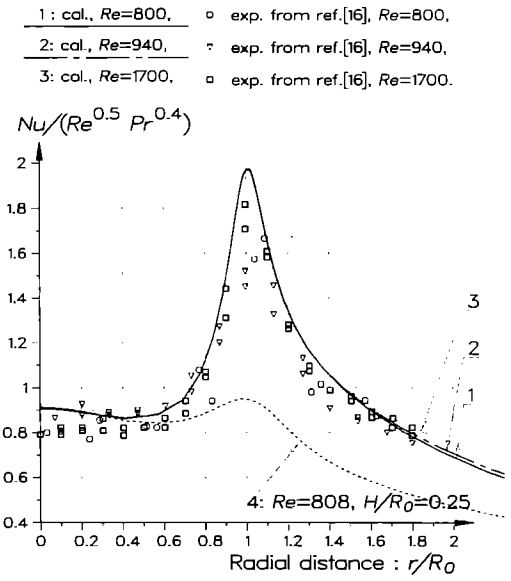

FIG. 14. Local Nusselt number profile on the substrate surface, comparison of the calculated values with experimental data, $Pr = 0.6904$.

$$\frac{Nu}{Re^{0.5}\,Pr^{0.4}} = 0.8958 - 6.982\times10^{-2}\left(\frac{r}{R_0}\right) - 0.4883\left(\frac{r}{R_0}\right)^2 + 0.3548\left(\frac{r}{R_0}\right)^3 - 0.1162\left(\frac{r}{R_0}\right)^4 + 2.093\times10^{-2}\left(\frac{r}{R_0}\right)^5 - 2.132\times10^{-3}\left(\frac{r}{R_0}\right)^6 + 1.150\times10^{-4}\left(\frac{r}{R_0}\right)^7 - 2.553\times10^{-6}\left(\frac{r}{R_0}\right)^8 \quad (14)$$

valid for $Re \geqslant 375$, $0.5 \leqslant Pr \leqslant 5$, $H/R_0 \geqslant 1$, $r/R_0 \leqslant 10$, and for small temperature difference.

When a small nozzle–substrate distance is used (Fig. 14) the Nusselt number profile presents large variations with the dimensionless distance H/R_0, and no simple correlation is available. Nevertheless, its maximum value is always reached at $r/R_0 = 1$. The agreement between calculated and experimental Nusselt number profiles for a nozzle–substrate distance $H/R_0 = 0.1$ is very satisfactory for the three Reynolds numbers $Re = 800$, 940, 1700 (curves 1, 2, 3) considered. These curves almost superpose for r/R_0 ranging from 0 to 2, which is an additional confirmation of the $Nu = f(Re^{0.5})$ dependence.

CONCLUSION

A model has been developed for the calculation of fluid flow and heat transfer occurring in a non-confined jet impinging on a heated surface. The good agreement between our calculation and the experimental data of Scholtz is an indication of its predictive capability in isothermal conditions.

The variation of the heat transfer has been numerically investigated as a function of various parameters such as Reynolds and Froude numbers, distance between nozzle exit and substrate, and direction of the jet with respect to the gravity field. A similar dependence of the local Nusselt number on the Reynolds number and the temperature of the substrate is observed. Both high Reynolds number and low temperatures increase the Nusselt number at the stagnation point, though an annular maximum is developed with detrimental effect at the centre in opposite conditions. Whatever the direction of the jet, the natural convection has detrimental effects on the heat transfer at the stagnation point for substrate temperatures exceeding 328 K when $Fr = 10.2$. However, the local Nusselt number at the periphery of the jet is enhanced.

For a small difference between the initial gas temperature and the substrate temperature, the calculated Nusselt number is in good agreement with that obtained from extrapolation of experimental mass transfer data by the use of the Chilton–Colburn ana-

logy. Moreover, the numerical solution describes very well the non-monotonous radial variation of the local Nusselt number experimentally determined for small nozzle–substrate distances. We confirmed that the Nusselt number is essentially dependent on the square root of the Reynolds number, as deduced from an analytical solution neglecting natural convection.

For a large difference between the initial gas temperature and the substrate temperature, and at low Reynolds number, the Nusselt number is considerably influenced by natural convection and the $Re^{0.5}$ dependence does not hold any more. As no experimental results were available for comparison in the large temperature difference case, an experimental confirmation of the model has still to be carried out.

This model will be completed by the mass transfer equations in order to take into account both homogeneous and heterogeneous chemical reactions.

Acknowledgements—The authors thank Dr G. Arnaud from Lab. des Systèmes Thermiques and Energétiques at Université of Poitiers (France) for helpful discussions.

REFERENCES

1. K. F. Jensen, Modelling of chemical vapor deposition reactors (Edited by C. H. J. van den Brekel, G. W. Cullen, J. M. Blocher, P. Rai-Choudhury and Mc. D. Robinson), *Proceedings of the IX International Conference on CVD Cincinatti U.S.A.*, pp. 3–20 (1984).
2. G. L. Tuve, Air velocities in ventilating jets, *Heating; Piping and Air Conditioning, The American Society of Heating and Ventilating Engineers, Journal Section*, pp. 181–191 (1953).
3. H. G. Elrod, Jr, Computation charts and theory for rectangular and circular jets, *Heating; Piping and Air Conditioning, The American Society of Heating and Ventilating Engineers, Journal Section*, pp. 149–155 (1954).
4. M. B. Donald and H. Singer, Entrainment in turbulent fluids jets, *Trans. Instn Chem. Engrs* **37**, 255–267 (1959).
5. P. Hrycak, Heat transfer from round impinging jets to a flat plate, *Int. J. Heat Mass Transfer* **26**, 1857–1865 (1983).
6. R. Gardon and J. Cahit Akrifat, The role of turbulence in determining the heat-transfer characteristics of impinging jets, *Int. J. Heat Mass Transfer* **8**, 1261–1272 (1965).
7. E. M. Sparrow, Z. X. Xu and L. F. A. Azevedo, Heat (mass) transfer for circular jet impinging on a confined disk with annular collection of the spent air, *J. Heat Transfer* **109**, 329–335 (1987).
8. H. Martin, D. B. Spalding, S. Whitaker and H. H. Winter, *Adv. Heat Transfer* **13**, 1–61 (1977).
9. H. R. Vallentine, *Applied Hydrodynamics*. Butterworth, London (1969).
10. M. P. du Plessis, R. L. Wang and S. Tsang, Development of a submerged round laminar jet from an initially parabolic profile, *J. Dynamics Systems Measurement and Controls, Transactions of the ASME*, 1–7 (1973).
11. H. Schlichting, *Boundary Layer Theory* (6th Edition). McGraw-Hill, New York (1968).
12. D. T. Chin and C. H. Tsang, Mass transfer to an impinging jet electrode, *J. Electrochem. Soc.* **125**, 1461–1470 (1978).
13. R. Srivastava and D. E. Rosner, A new approach to the correlation of boundary layer mass transfer rates with thermal diffusion and/or variable properties, *Int. J. Heat Mass Transfer* **22**, 1281–1294 (1979).
14. G. Wahl, Hydrodynamic description of CVD processes, *Thin Solid Films* **40**, 13–26 (1977).
15. C. Houtman, D. B. Graves and K. F. Jensen, CVD in stagnation point flow, *J. Electrochem. Soc.* **133**, 961–970 (1986).
16. M. T. Scholtz and O. Trass, Mass transfer in a nonuniform impinging jet, *A.I.Ch.E. Jl* **16**, 82–96 (1970).
17. M. D. Deshpande and R. N. Vaishnav, Submerged laminar jet impingement on a plane, *J. Fluid Mech.* **114**, 213–236 (1982).
18. T. D. Yuan, J. A. Liburdy and T. Wang, Buoyancy effects on laminar impinging jets, *Int. J. Heat Mass Transfer* **31**, 2137–2145 (1988).
19. S. V. Patankar, *Numerical Heat Transfer and Fluid Flow*. McGraw-Hill, New York (1980).
20. E. A. Spiegel and G. Veronis, On the Boussinesq approximation for a compressible fluid, *Astrophys. J.* **131**, 442–447 (1960).
21. D. D. Gray and A. Giorgini, The validity of the Boussinesq approximation for liquids and gases, *Int. J. Heat Mass Transfer* **19**, 545–551 (1976).
22. J. M. Mihaijan, A rigorous exposition of the Boussinesq approximation applicable to a thin layer of fluids, *Astrophys. J.* **136**, 1126 (1962).
23. R. Byron Bird, W. E. Stewart and E. N. Lightfoot, *Transport Phenomena*. Wiley, New York (1960).
24. S. Mikhail, S. M. Morcos, M. M. M. Abul-Ellail and W. S. Ghaly, Numerical prediction of flow field and heat transfer from a row of laminar slot jets impinging on a flat plate, *Proceedings of the Seventh International Heat Transfer Conference* **3**, 337–382 (1982).
25. J. O. Hirschfelder, C. F. Curtiss and R. Byron Bird, *Molecular Theory of Gases and Liquids* (2nd Edition). Wiley, London (1964).
26. R. C. Reid, J. M. Prausnitz and T. K. Sherwood, *The Properties of Gases and Liquids* (3rd Edition). McGraw-Hill, New York (1977).
27. R. C. Weast, M. J. Astle and W. H. Beyer, *CRC Handbook of Chemistry and Physics* (66th Edition). CRC Press, B-138 (1985–1986).